Mechanical behavior of layered and functional graphene material distributions under thermo-mechanical loading

Jiahe Zhao [a] , Yu Zhang [b*]
a College of Energy and Power Engineering, Nanjing University of Aeronautics and Astronautics, Nanjing 210016, China
b Department of Civil Engineering, Zhejiang University, Hangzhou 310058, China
* Corresponding author, E-mail: YuZhangg@outlook.com

Abstract: Current research efforts have yet to comprehensively compare the thermo-mechanical performance disparities between layered and power-law graded graphene-reinforced composites, particularly regarding structural optimization under operational constraints. To address this gap, this investigation establishes a model methodology for composite analysis, synergistically integrating the Halpin-Tsai micromechanical constitutive modeling framework with Maxwell-Eucken multiphase homogenization principles. A nonlinear finite element framework was established based on the simplified first-order shear deformation theory (S-FSDT), and the numerical solution of the bending response of the plate is obtained by Newton-Raphson iteration. The proposed models were validated against existing literature. A systematic study was conducted on the thermodynamic coupling properties of layered and power-law graded graphene distributions with various pore types. Parametric comparisons showed that symmetric surface-enriched distributions achieved optimal performance in all configurations. The power-law graded type demonstrated superior reinforcement efficacy over the layered design. This study reveals the synergy between pore distribution and graphene gradient design, offering theoretical support for optimizing lightweight high-stiffness composites.

Keywords: Layered graphene; Power-law graded graphene; S-FSDT; Thermo-Mechanical loads; FEM

1. Introduction

Graphene has emerged as a transformative reinforcement in composites due to its exceptional mechanical and thermal properties. Its ultra-high mechanical properties [1] and excellent thermal conductivity [2] have enabled it to show great potential in high-end fields such as lightweight thermal protection systems in aerospace, new energy automobile battery assemblies, flexible electronic devices, biomedical sensors, and other high-end fields. Compared to carbon nanotubes (CNTs), graphene platelets (GPLs) offer better interfacial bonding and cost efficiency. Through functionally graded distribution (FGD), the spatial concentration of GPLs can be precisely tailored to optimize local material performance [3]. Current research primarily focuses on two distribution types: layered graphene-reinforced composites and power-law graded composites based on trigonometric functions and volume fractions.

In research on layered graphene-reinforced composites, non-uniform gradient distributions have been shown to improve overall performance. Song et al. [4] demonstrate

that the strategic dispersion of more square-shaped graphene platelets, composed of FG-X distribution, is the most effective method for enhancing the plate's natural frequencies and significantly reducing dynamic deflections. Tao et al. [5] indicate that the FG-X configuration exhibits the optimal load-deflection response in the post-buckling of cylindrical and spherical shell plates made from layer graphene reinforced composite. Thai et al. [6] highlight the superior reinforcement efficacy of the FG-X distribution mode. At a fixed GPL mass fraction, the FG-X configuration attains the highest natural frequency. In the study of stress distribution, Jin et al. [7] analyzed four FG-CNTRC laminated plates with piezoelectric layers, revealing that in-plane stress varies linearly through the thickness under uniform distribution (UD) conditions but nonlinearly for functionally graded (FG-X, FG-O, FG-V) configurations. Van-Loi et al. [8] found that for the FG-X distribution pattern with 2% W_{GPL}, the GPL-reinforced P-FGM composite plates exhibit a 32.43% increase in normalized critical buckling load and a 24.48% reduction in normalized central deflection.

Research on power-law graded graphene reinforced composites has demonstrated that surface-enriched GPL distributions (e.g., GS-type) significantly enhance flexural stiffness and critical buckling loads. Theoretical analyses confirm that porosity distribution critically modulates mechanical properties through localized density variations, driving research on GPL-porosity synergy. For example, Do et al. [10] demonstrated that FGA-type GPL distribution combined with P1-type porosity achieves superior thermal buckling resistance. She et al. [11] systematically studied conical and cylindrical shells, showing that increased GPL content enhances resonance frequencies, amplifies nonlinear hardening behavior, and improves vibration resistance via GPL-A/Porosity-Ix configurations. Liu et al. [12] reported that GS/GA-type GPL gradations optimize thermoelastic response, reducing thermal deformation. In piezoelectric-bonded porous functionally graded plates [14], 1.0 wt.% GPLs dispersion maximized natural frequency enhancement. Chen et al. [17] found that the natural frequency of the symmetrically distributed pore-graphene combination is slightly different from that of the linear temperature field under the nonlinear temperature field, while the asymmetric combination shows a significant frequency change. Zhang et al. [16] quantified thermo-electro-mechanical coupling effects in porous GPL-reinforced plates, showing that GS-PS configurations enhance stiffness and sustain higher nonlinear frequencies. Tu et al. [17] revealed size-dependent nonlinear dynamics in GPL-reinforced microporous plates under thermal gradients, achieving 35% amplitude reduction through optimized nanofiller geometry. Huang et al. Huang [18] et al. optimized rotating sandwich annular plates with functionally graded porous cores, demonstrating that surface-dense porosity and GPL enrichment significantly improve structural stiffness and natural frequencies.

It is evident that the current research predominantly centers on the elastic behavior of materials, such as vibration and bending. However, systematic investigations into non-elastic behaviors—such as plastic deformation and fatigue crack propagation—are still lacking [3]. Current research in this field is predominantly confined to studies by Song et al. [20][21]. Current research predominantly examines either power-law graded or layered graphene distributions within composites, yet a systematic comparison between these two types is lacking. While much of the literature highlights the

enhancement of thermomechanical properties through gradient distribution, there is a scarcity of comprehensive comparisons between these two types of composites. This limitation impedes the quantitative evaluation of gradient design optimization and the selection of appropriate graphene distribution types for engineering applications. This study addresses the gap by investigating the geometrically nonlinear responses of porous plates reinforced with both distribution patterns. Based on S-FSDT, Halpin–Tsai model, and Maxwell–Eucken equation, numerical models are established and validated. Parametric studies reveal how porosity and graphene distribution affect material properties, thermal behavior, and bending performance. Results demonstrate that power-law graded graphene (GS) yields higher stiffness than layered functionally graded structures (FG-X), providing key insights for optimizing graphene reinforcement in engineering applications.

2. Modeling of two distinct graphene types

In this section, we construct two different graphene models. In 2.1 and 2.2, we construct pure graphene composite panels without pores, and in 2.3, we build two types of graphene-reinforced composite panels with pores, where z_m is the distance from the physical midplane to the geometric midplane.

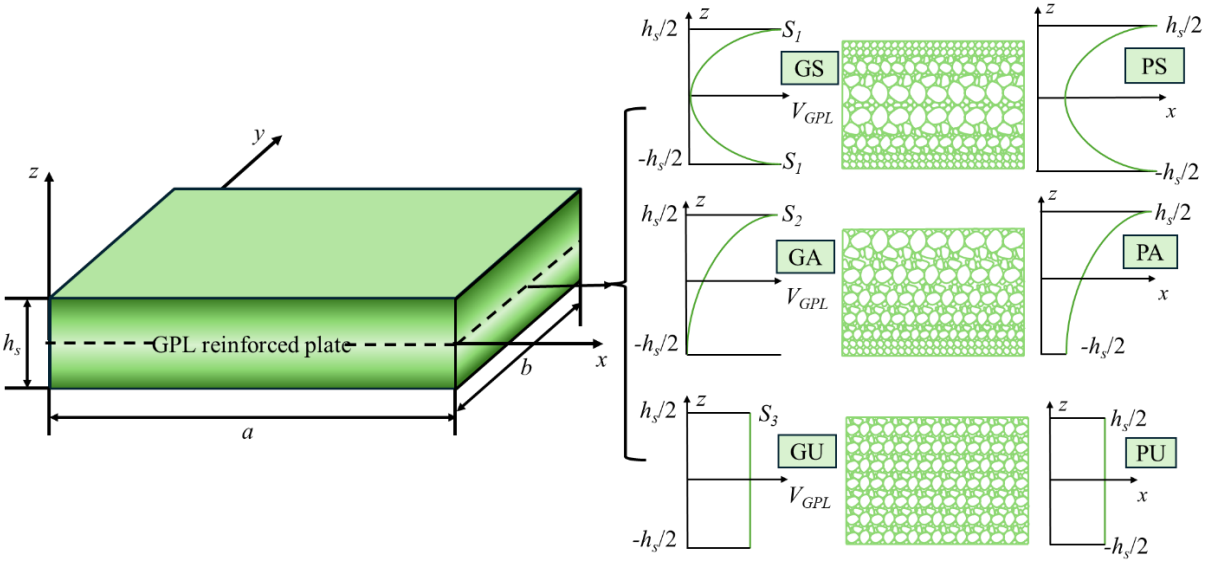

(a) Power-law graded graphene and three types of porosity distribution

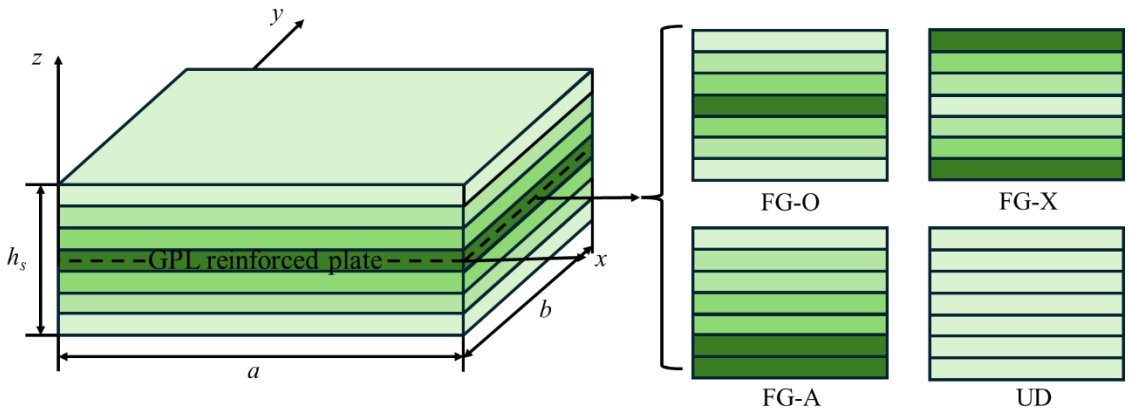

(b) Layered Graphene

Fig.1. Two types of graphene and pore types

2.1. Power-law graded graphene

The power-law graded graphene composite plates of this model are shown in Fig.1(a), featuring characteristic dimensions($a \times b \times h_s$). Three distinct GPL dispersion modes were implemented through the plate's thickness domain GS(Symmetric nonlinear distribution with mid-plane concentration), GA(Asymmetric gradient distribution towards the top surface), and GU(Uniform distribution).

It is assumed that the three types of volume distribution functions for GPL in a purely graphene-reinforced plate can be expressed as[12]:

$$V_{\mathrm{GPL}}(z)=\begin{cases}S_1(1-\cos(\pi z/h_s)) & \mathrm{GS}\\ S_2(1-(\cos(\pi z/(2h_s)+\pi/4)) & \mathrm{GA}\\ S_3 & \mathrm{GU}\end{cases} \tag{1}$$

where S_1, S_2 and S_3 are volume peaks corresponding to different GPL volume distributions under no pore. These parameters can be determined using the relationship between wight fraction and volume fraction as the following equation.

$$\int_{-h_s/2}^{h_s/2} V_{\mathrm{GPL}} = h_s \frac{W_{\mathrm{GPL}}\rho_{\mathrm{m}}}{W_{\mathrm{GPL}}\rho_{\mathrm{m}}+\rho_{\mathrm{GPL}}-W_{\mathrm{GPL}}\rho_{\mathrm{GPL}}} \tag{2}$$

where W_{GPL} denotes the wight fraction of graphene, ρ_m and ρ_{GPL} are the densities of substrate matrix materials and graphene sheets.

To obtain the effective elastic modulus of power-law graded graphene composites, we use the micromechanics of the Halpin-Tsai model. According to the mixing law, the density, Poisson's ratio, and thermal expansion coefficient of the final material can be expressed as[16]:

$$E_{\mathrm{e}}=E_{\mathrm{m}}\left[\frac{5}{8}\left(\frac{1+\zeta_{\mathrm{W}}\lambda_{\mathrm{W}}V_{\mathrm{GPL}}}{1-\zeta_{\mathrm{W}}V_{\mathrm{GPL}}}\right)+\frac{3}{8}\left(\frac{1+\zeta_{\mathrm{L}}\lambda_{\mathrm{L}}V_{\mathrm{GPL}}}{1-\zeta_{\mathrm{L}}V_{\mathrm{GPL}}}\right)\right] \tag{3}$$

$$\rho_{\mathrm{e}}=\rho_{\mathrm{GPL}}V_{\mathrm{GPL}}+\rho_{\mathrm{m}}(1-V_{\mathrm{GPL}}) \tag{4}$$

$$\mu_{\mathrm{e}}=\mu_{\mathrm{GPL}}V_{\mathrm{GPL}}+\mu_{\mathrm{m}}(1-V_{\mathrm{GPL}}) \tag{5}$$

$$\alpha_{\mathrm{e}}=\alpha_{\mathrm{GPL}}V_{\mathrm{GPL}}+\alpha_{\mathrm{m}}(1-V_{\mathrm{GPL}}) \tag{6}$$

where E_{m}, μ_{m} denote the modulus of elasticity and Poisson's ratio of the matrix, respectively, while $\lambda_{\mathrm{W}}^{\mathrm{GPL}}$, $\lambda_{\mathrm{L}}^{\mathrm{GPL}}$, $\zeta_{\mathrm{W}}^{\mathrm{GPL}}$, $\zeta_{\mathrm{L}}^{\mathrm{GPL}}$ are related to the average length l_{GPL}; average thickness h_{GPL} average width w_{GPL} of the GPL, calculated as follows

$$\begin{aligned}\lambda_W&=\frac{(\mathrm{E}_{\mathrm{GPL}}/E_{\mathrm{m}})-1}{(E_{\mathrm{GPL}}/E_{\mathrm{m}})+\zeta_{\mathrm{W}}},\zeta_{\mathrm{W}}=\frac{2w_{\mathrm{GPL}}}{h_{\mathrm{GPL}}}\\ \lambda_L&=\frac{(E_{\mathrm{GPL}}/E_{\mathrm{m}})-1}{(E_{\mathrm{GPL}}/E_{\mathrm{m}})+\zeta_{\mathrm{L}}},\zeta_L=\frac{2l_{\mathrm{GPL}}}{h_{\mathrm{GPL}}}\end{aligned} \tag{7}$$

For the thermal conductivity in composites, firstly, using micromechanical modeling, the thermal conductivity of GPL composites in the absence of holes is described by the following equations[14].

$$k_{\mathrm{e}}=k_{\mathrm{m}}\left[\frac{V_{\mathrm{GPL}}}{3}\left(\frac{2}{(1-Y)/2+1/(k_z/k_{\mathrm{m}}-1)}+\frac{2}{Y+1/(k_{\mathrm{x}}/k_{\mathrm{m}}-1)}\right)+1\right] \tag{8}$$

where k_m denotes the thermal conductivity of the base material, and

$$k_z = \frac{k_{\mathrm{GPL}}}{2R_k k_{\mathrm{GPL}}/t_{\mathrm{GPL}}+1}, k_{\mathrm{x}} = \frac{k_{\mathrm{GPL}}}{2R_k k_{\mathrm{GPL}}/l_{\mathrm{GPL}}+1} \tag{9}$$

$$Y = \frac{\ln\left[\left(d+\sqrt{d^2-1}\right)d\right]}{\sqrt[3]{\left(d^2-1\right)^3}} - \frac{1}{d^2-1} \tag{10}$$

where $d = l_{\mathrm{GPL}}/h_{\mathrm{GPL}}$, R_k are the average interfacial thermal resistances between the matrix material and the GPL, and k_{GPL} is the thermal conductivity of the GPL.

2.2. Layered Graphene

The present model, as in Fig. 1(b), is a multilayer functional gradient graphene composite plate with thickness h_s and length and width a and b, respectively. The plate has a total of N_L layers, each with a thickness of h_s/N_L. It is assumed that the GPL is uniformly filled in the matrix of each layer, and the weight score of the GPL varies depending on the layer. Fig.1(a) shows four GPL distribution modes.

The weight fraction i of layer $W_{\mathrm{GPL}}^{(i)}$ GPL is expressed as follows [6].

$$W_{\mathrm{GPL}}^{(i)} = \begin{cases} \dfrac{2W_{\mathrm{GPL}}\left(\left|2i-N_L-1\right|+1\right)}{(N_L+2)} & \text{(FG-X)} \\ \dfrac{2W_{\mathrm{GPL}}\left(\left|2i-N_L-1\right|+N_L+1\right)}{(N_L+2)} & \text{(FG-O)} \\ 2W_{\mathrm{GPL}}i/(N_L+1) & \text{(FG-A)} \\ W_{\mathrm{GPL}} & \text{(UD)} \end{cases} \tag{11}$$

where the volume fraction of GPLs in layer i is

$$V_{\mathrm{GPL}}^{(i)} = \frac{\rho_{\mathrm{m}} W_{\mathrm{GPL}}^{(i)}}{\rho_{\mathrm{m}} W_{\mathrm{GPL}}^{(i)} + \rho_{GPL}\left(1-W_{\mathrm{GPL}}^{(i)}\right)} \tag{12}$$

where ρ_{GPL} and ρ_{m} are the densities of the GPLs and the matrix, respectively.

The forms of material parameters, such as $E^{(i)}$, $\rho^{(\mathrm{i})}$, $\mu^{(\mathrm{i})}$ and $k^{(i)}$ are the same as those of power-law graphene.

2.3. Material properties of plates after adding pores

In this section, we model the material of plates with pore distributions added to the already graphene reinforced composite plates, with three types of pore distributions, as shown in Fig. 1(a), with distribution functions of

$$\phi(z)=\begin{cases}\cos(\pi z/h_s) & \text{PS}\\ \cos(\pi z/(2h_s)+\pi/4) & \text{PA}\\ \varphi & \text{PU}\end{cases} \tag{13}$$

The material parameters of the porous graphene sheet reinforced composite, including elastic modulus E; density ρ and Poisson's ratio μ; can be expressed as follows:

$$\begin{cases}E(z)=E_{\max}\left[1-e_0\phi(z)\right]\\ \rho(z)=\rho_{\max}\left[1-e_{\mathrm{m}}\phi(z)\right]\end{cases} \tag{14}$$

where e_0 is the average pore coefficient $e_0=1-E_{\max}/E_{\min}$. $E_{\max}$ and $E_{\min}$ denote the effective maximum and minimum modulus of elasticity of the material, respectively, while in this section $E_{\max}$ and $\rho_{\max}$ are the material parameters of the pure graphene reinforced composite plate. Poisson's ratio μ is expressed as:

$$\mu(z)=0.221\hat{p}+\mu_{\max}(0.342\hat{p}^2-1.121\hat{p}+1) \tag{15}$$

similarly $\mu_{\max}$ is also the Poisson's ratio of a non-porous graphene reinforced composite plate, where $\tilde{p}$ and e_{m} can be solved using a homogenization method based on the assumption of representative volume elements .

$$\begin{cases}\hat{p}=1.121-\sqrt[2.3]{1-e_0\phi(z)}\\ e_{\mathrm{m}}=\dfrac{1.121-\sqrt[2.3]{1-e_0\phi(z)}}{\phi(z)}\end{cases} \tag{16}$$

Meanwhile, the modulus of elasticity and density in Eq. (14) satisfy the following relationship, while the pore coefficient is required to be in the range of 0 to 0.9618 [14]:

$$\frac{E(z)}{E_{\max}}=\left(\frac{\rho(z)/\rho_{\max}+0.121}{1.121}\right)^{2.3}\left(0.15<\frac{\rho(z)}{\rho_{\max}}<1\right) \tag{17}$$

Assuming that the total mass of the final enhanced plate plates with different porosity distributions are equal,

$$M=\int_{-h_s/2}^{h_s/2}\rho(z)\mathrm{d}z=\int_{-h_s/2}^{h_s/2}\rho_{\max}(1-\tilde{p})\mathrm{d}z \tag{18}$$

The uniform distribution of porosity for the combined Eqs. (14), (16), and (18) can be expressed as

$$\varphi=\frac{1}{e_0}\left(1-\left(\frac{M/h_s+0.121}{1.121}\right)^{2.3}\right) \tag{19}$$

where $\tilde{M} = M / \rho_{\max} = \int_{-h_s/2}^{h_s/2} (1-\tilde{p}) \mathrm{d}z$.

In addition, the presence of pores also affects the graphene volume fraction, and the equation for the relationship between its volume fraction and mass fraction is then as follows [12]

$$\int_{-h_s/2}^{h_s/2} V_{\mathrm{GPL}} \left[1-e_{\mathrm{m}}\phi(z)\right] \mathrm{d}z = \frac{W_{\mathrm{GPL}}\rho_{\mathrm{m}}}{W_{\mathrm{GPL}}\rho_{\mathrm{m}} + \rho_{\mathrm{GPL}} - W_{\mathrm{GPL}}\rho_{\mathrm{GPL}}} \int_{-h_s/2}^{h_s/2} \left[1-e_{\mathrm{m}}\phi(z)\right] \mathrm{d}z \tag{20}$$

Similarly, pores can also influence the thermal conductivity, which can be determined using the Maxwell-Eucken equation[14], as shown below:

$$k(z) = k_{\mathrm{e}}(z) \left[\frac{k_{\mathrm{air}} + 2k_{\mathrm{e}}(z) + 2e_0\phi(z)\left(k_{\mathrm{air}} - k_{\mathrm{e}}(z)\right)}{k_{\mathrm{air}} + 2k_{\mathrm{e}}(z) - e_0\phi(z)\left(k_{\mathrm{air}} - k_{\mathrm{e}}(z)\right)} \right] \tag{21}$$

where $k(z)$ is the thermal conductivity of the nonporous graphene reinforced composite sheet and k_{air} is the thermal conductivity of air.

Assuming that the temperature changes only along the thickness of the plate, the 1D steady-state heat transfer equation [23] is:

$$-\frac{\mathrm{d}}{\mathrm{d}z}\left(k(z)\frac{\mathrm{d}T}{\mathrm{d}z} \right) = 0 \tag{22}$$

Using the first kind of boundary conditions, the temperature distribution through the thickness direction is expressed as:

$$T(z) = T_l + \frac{(T_u - T_l)}{\int_{-h_s/2}^{h_s/2} \frac{1}{k(z)} \mathrm{d}z} \int_{-h_s/2}^{z} \frac{1}{k(z)} \mathrm{d}z \tag{23}$$

where T_u and T_l are the temperatures at $z = h_s/2$ and $z = -h_s/2$, respectively

3. Nonlinear finite element of plate

3.1. Geometric equations

The simplified first-order shear deformation theory (S-FSDT) effectively avoids shear locking compared to conventional FSDT, while achieving higher computational efficiency than higher-order theories (HSDT) due to its reduced degrees of freedom. This approach differs from the one-section shear theory in that, within the S-FSDT framework, deflection is articulated in terms of both bending deflection w_b and shear deflection w_s, i.e. $w_0 = w_b + w_s$, In this formulation, the two angular variables in the first-order shear deformation are represented by the partial derivatives of the bending terms, i.e., $\beta_x = -\partial w_b / \partial x, \beta_y = -\partial w_b / \partial y$.

The displacement of any point in the plate is:

$$\begin{cases} u(x,y,z) = u_0(x,y) - (z - z_m)\partial w_b / \partial x \\ v(x,y,z) = v_0(x,y) - (z - z_m)\partial w_b / \partial y \\ w(x,y,z) = w_s(x,y) + w_b(x,y) \end{cases} \tag{24}$$

The above equation is converted to the matrix $\boldsymbol{u} = \boldsymbol{Z}_{\mathrm{u}}\boldsymbol{u}_0$. $\boldsymbol{u}_0 = \{u_0 \quad v_0 \quad w_b \quad w_s\}^{\mathrm{T}}$, and $\boldsymbol{Z}_{\mathrm{u}}$ is given by the following equation:

$$\boldsymbol{Z}_{\mathrm{u}} = \begin{bmatrix} 1 & 0 & -(z - z_m)\partial/\partial x & 0 \\ 0 & 1 & -(z - z_m)\partial/\partial y & 0 \\ 0 & 0 & 1 & 1 \end{bmatrix} \tag{25}$$

By employing the Von-Karman nonlinear theory [22], the strain-displacement relationship of the plate can be formulated as follows:

$$\overline{\boldsymbol{\varepsilon}} = \boldsymbol{H}_{\mathrm{s}}\hat{\boldsymbol{\varepsilon}} = \begin{bmatrix} \boldsymbol{H}_{\mathrm{s1}} & \boldsymbol{H}_{\mathrm{s3}} & 0 \\ 0 & 0 & \boldsymbol{H}_{\mathrm{s3}} \end{bmatrix} \begin{Bmatrix} \boldsymbol{\varepsilon}_m + \boldsymbol{\varepsilon}_{NL} \\ \boldsymbol{\varepsilon}_b \\ \boldsymbol{\varepsilon}_s \end{Bmatrix} = \begin{Bmatrix} u_{,x} + \frac{w_{,x}^2}{2} \\ v_{,y} + \frac{w_{,y}^2}{2} \\ u_{,y} + w_{,x}w_{,y} + v_{,x} \\ w_{,x} + u_{,z} \\ w_{,y} + v_{,z} \end{Bmatrix} \tag{26}$$

where

$$\boldsymbol{\varepsilon}_m = \{u_{0,x} \quad v_{0,x} \quad u_{0,y} + v_{0,x}\}^{\mathrm{T}} \tag{27}$$

$$\boldsymbol{\varepsilon}_b = \{w_{b,xx} \quad w_{b,yy} \quad 2w_{b,xy}\}^{\mathrm{T}} \tag{28}$$

$$\boldsymbol{\varepsilon}_s = \{w_{s,x} \quad w_{s,y}\}^{\mathrm{T}} \tag{29}$$

$$\boldsymbol{\varepsilon}_{\mathrm{NL}} = \frac{1}{2}\overline{\boldsymbol{A}}\boldsymbol{\theta} = \frac{1}{2}\begin{Bmatrix} (w_{,x})^2 \\ (w_{,y})^2 \\ 2w_{,x}w_{,y} \end{Bmatrix}, \boldsymbol{\theta} = \begin{Bmatrix} w_{b,x} + w_{s,x} \\ w_{b,y} + w_{s,y} \end{Bmatrix}, \overline{\boldsymbol{A}} = \begin{Bmatrix} w_{b,x} + w_{s,x} & 0 \\ 0 & w_{b,y} + w_{s,y} \\ w_{b,y} + w_{s,y} & w_{b,x} + w_{s,x} \end{Bmatrix} \tag{30}$$

$$\boldsymbol{H}_{\mathrm{S1}} = \begin{bmatrix} 1 & 0 & 0 \\ 0 & 1 & 0 \\ 0 & 0 & 1 \end{bmatrix}, \boldsymbol{H}_{\mathrm{S2}} = \begin{bmatrix} z - z_m & 0 & 0 \\ 0 & z - z_m & 0 \\ 0 & 0 & z - z_m \end{bmatrix}, \boldsymbol{H}_{\mathrm{S3}} = \begin{Bmatrix} 1 & 0 \\ 0 & 1 \end{Bmatrix} \tag{31}$$

The plate's constitutive relations are formulated as [24]

$$\boldsymbol{\sigma} = \boldsymbol{Q}\overline{\boldsymbol{\varepsilon}} \tag{32}$$

where $\boldsymbol{\sigma}$ is the stress vector; $\boldsymbol{Q}$ denotes the matrix of elastic constants, which can be expressed as[32]

$$\boldsymbol{Q}=\begin{bmatrix} Q_{11} & Q_{12} & 0 & 0 & 0 \\ Q_{21} & Q_{22} & 0 & 0 & 0 \\ 0 & 0 & Q_{66} & 0 & 0 \\ 0 & 0 & 0 & Q_{55} & 0 \\ 0 & 0 & 0 & 0 & Q_{44} \end{bmatrix} \tag{33}$$

For a perforated multilayer functional gradient graphene composite sheet, Eq. (33) then represents the matrix of elastic constants for each layer, and the elements in $Q^{(i)}$ for layer *i* are as follows

$$\begin{aligned} Q_{11}^{(i)}=Q_{22}^{(i)}&=\frac{E^{(i)}}{1-(\mu^{(i)})^2},\quad Q_{12}^{(i)}=Q_{21}^{(i)}=\frac{\mu^{(i)}E^{(i)}}{1-(\nu^{(i)})^2} \\ Q_{66}^{(i)}=Q_{55}^{(i)}&=Q_{44}^{(i)}=\frac{E^{(i)}}{2(1+\mu^{(i)})} \end{aligned} \tag{34}$$

3.2. Nonlinear finite element equations

In this study, a four-node rectangular planar stress cell is utilized to address the problem. The displacement of any point within the plate domain can be represented as

$$\boldsymbol{u}_0=\begin{Bmatrix} u_0 & v_0 & w_b & w_s \end{Bmatrix}^{\mathrm{T}}=\sum_{N=1}^{4}\boldsymbol{R}_N\boldsymbol{q}_N \tag{35}$$

where $\boldsymbol{q}_N$ denotes the displacement vector of node $N(N=1,2,3,4)$ and $\boldsymbol{q}_N=\begin{Bmatrix} u_N & v_N & w_{bN} & w_{sN} \end{Bmatrix}^{\mathrm{T}}$. $\boldsymbol{R}_N$ denotes the shape function. The strain can be expressed as

$$\hat{\boldsymbol{\varepsilon}}=\begin{Bmatrix} \boldsymbol{\varepsilon}_{\mathrm{m}} \\ \boldsymbol{\varepsilon}_{\mathrm{b}} \\ \boldsymbol{\varepsilon}_{\mathrm{s}} \end{Bmatrix}+\begin{Bmatrix} \boldsymbol{\varepsilon}_{\mathrm{NL}} \\ 0 \\ 0 \end{Bmatrix}=\sum_{N=1}^{4}\left(\begin{Bmatrix} \boldsymbol{B}_I^{\mathrm{m}} \\ \boldsymbol{B}_I^{\mathrm{b}} \\ \boldsymbol{B}_{\mathrm{I}}^{\mathrm{s}} \end{Bmatrix}+\begin{Bmatrix} \boldsymbol{B}_I^{\mathrm{NL}} \\ 0 \\ 0 \end{Bmatrix}\right)\boldsymbol{q}_N=\left(\boldsymbol{B}_{\mathrm{L}}+\boldsymbol{B}_{\mathrm{NL}}\right)\boldsymbol{q}^e \tag{36}$$

where

$$\boldsymbol{B}_N^{\mathrm{m}}=\begin{bmatrix} R_{N,x} & 0 & 0 & 0 \\ 0 & R_{N,y} & 0 & 0 \\ R_{N,y} & R_{N,x} & 0 & 0 \end{bmatrix},\boldsymbol{B}_N^{b}=\begin{bmatrix} 0 & 0 & R_{N,xx} & 0 \\ 0 & 0 & R_{N,yy} & 0 \\ 0 & 0 & 2R_{N,xy} & 0 \end{bmatrix},\boldsymbol{B}_N^{s}=\begin{bmatrix} 0 & 0 & 0 & R_{N,x} \\ 0 & 0 & 0 & R_{N,y} \end{bmatrix} \tag{37}$$

$$\boldsymbol{B}_N^{\mathrm{NL}}=\frac{1}{2}\overline{A}\boldsymbol{B}_N^{g} \tag{38}$$

at the same time

$$\boldsymbol{B}_N^{g}=\begin{bmatrix} 0 & 0 & R_{N,x} & R_{N,x} \\ 0 & 0 & R_{N,y} & R_{N,y} \end{bmatrix} \tag{39}$$

3.3. Nonlinear governing equations

This part establishes the nonlinear governing equations of the plate. According to the principle of virtual displacement, the total energy change of the plate can be derived from the following equation [28]:

$$\int_{t_2}^{t_1}\left(\delta W_{ext}+\delta U\right)\mathrm{d}t=0 \tag{40}$$

where U, W_{ext} denotes potential energy and external work respectively, they can be expressed as [22] respectively

$$\delta U=\int_V\left(\delta\overline{\boldsymbol{\varepsilon}}^{\mathrm{T}}\boldsymbol{\sigma}\right)\mathrm{d}V \tag{41}$$

$$\delta W_{\mathrm{ext}}=\int_\Omega\delta\boldsymbol{u}^{\mathrm{T}}\boldsymbol{f}_{us}\,\mathrm{d}\Omega+\sum\delta\boldsymbol{u}^{\mathrm{T}}\boldsymbol{f}_{uc}+\int_\Omega\delta\boldsymbol{u}^{\mathrm{T}}\boldsymbol{f}_{ub}\,\mathrm{d}V \tag{42}$$

where u denotes displacement; $\boldsymbol{f}_{us}$, $\boldsymbol{f}_{uc}$ and $\boldsymbol{f}_{ub}$ denote face, point, and body loads respectively. Finally, Eq. (26) and Eq. (32) are brought into Eq. (41), Eq. (24) is brought into Eq. (42), the element is assembled, and the geometric nonlinear equation is[12]

$$\left(\boldsymbol{K}_{uu}+\boldsymbol{K}_G\right)\Delta\boldsymbol{d}=\boldsymbol{F}_u-\boldsymbol{F}_{ui} \tag{43}$$

where the expressions for $\boldsymbol{K}_{uu}$, $\boldsymbol{K}_G$, $\boldsymbol{F}_u$ and $\boldsymbol{F}_{ut}$ in Eq. (43) are given in the Appendix .

4. Model Validation

The Newton-Raphson method[9] was employed to solve the governing equations for both layered and power-law graded graphene-reinforced panels. The accuracy of the nonlinear numerical approach was validated through comparisons with established literature benchmarks. The plates are simply supported, and all material parameters are provided in Table 1.

Table 1. Parameters of substrate materials and graphene materials

Material parameters	GPL	Aluminum	Zirconia	Epoxy
E (GPa)	1010	70	151	3
v	0.186	0.3	0.3	0.34
ρ (kg/m^3)	1062.5	2707	3000	1200
α(10^{-6}/K)	5	23	10	60
k (W/mK)	2000	204	2.09	0.2
R_k (10^{-9}/Km^2/W)	—	—	—	10

4.1. Temperature distribution

To ensure the accuracy of the temperature distribution among graphene-reinforced plates, we first compare and validate the temperature distributions in FGM (functionally graded material plates), several types of GPLs(W_{GPL} = 1.0 wt%), and porous materials, and under different temperature fields. We examine the temperature distribution of a plate with dimensions of 0.2×0.2×0.01 m³. Both the top and bottom temperatures of the

plate are provided in the figure. Fig. 2(a) presents the dimensionless through-thickness temperature distribution of an FGM plate, and Fig. 2(b) illustrates the temperature distribution of a porous GPLs-reinforced plate. The results demonstrate a close alignment with those reported by Reddy [29] and Liu et al. [12].

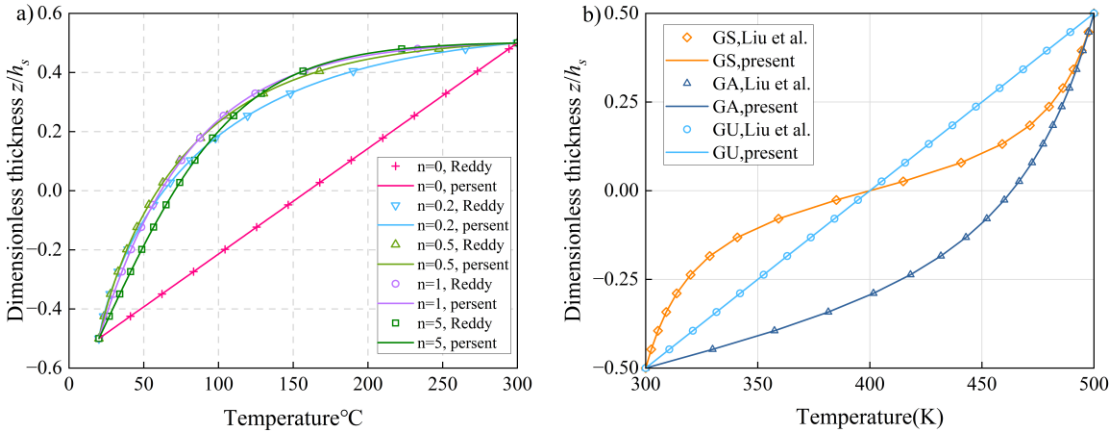

Fig. 2. Thickness temperature profiles of (a) FGM plates and (b) porous graphene platelets (GPL) reinforced epoxy composites.

4.2. Material distribution verification

In this section, we have simultaneously verified the elastic modulus distribution of layered graphene reinforced non-porous plates in the along-thickness direction, and also verified the thermal conductivities of plates with different pore and GPLs distribution patterns and non-porous GPL reinforced composite plates in the along-thickness direction. Fig.3 and Fig.4 are the same as the results of Thai et al. [5] and Liu et al. [12].

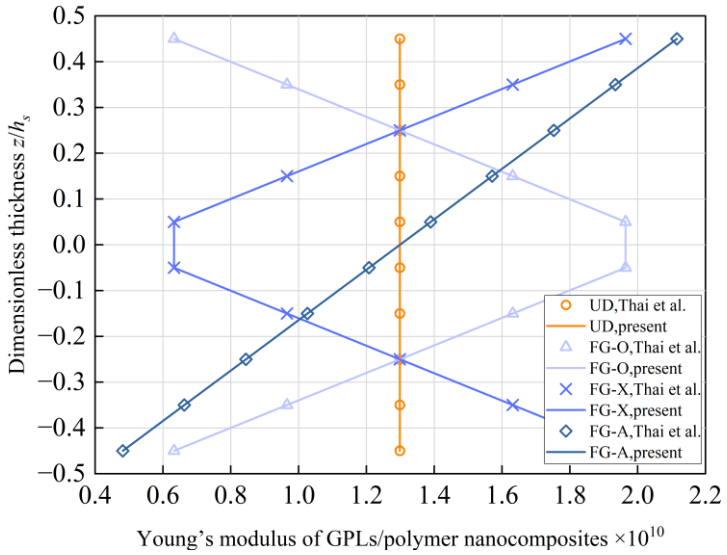

Fig. 3. Effects of four graphene distribution modes on Young's modulus of GPLs/Epoxy composites at $N_L = 10$.

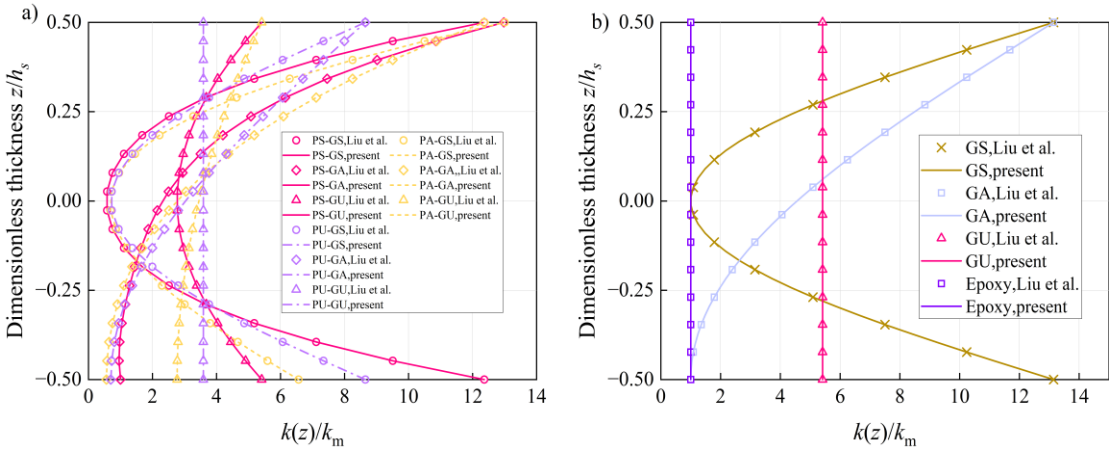

Fig. 4. Thermal conductivity through the thickness direction of (a) porous GPLs reinforced composite plates and (b) non-porous GPLs reinforced composite plates.

4.3. Nonlinear static bending verification

In this section, we investigate the nonlinear static bending response of a pure layered graphene reinforced plate under a uniform load of 500 kPa. We examine the connection between the number of layers, denoted as N_L, and the percentage variation in plate deflection (w_c/w_m) in Fig. 5, where w_c and w_m denote the central deflections of the plates with GPL(W_{GPL}=1.0 wt%) reinforcement and epoxy plate. Our computed results exhibit excellent agreement with those reported in [31], and it can also be seen that the deflection of the plate becomes stable with the increasing number of layers, so the number of layers we chose 25.

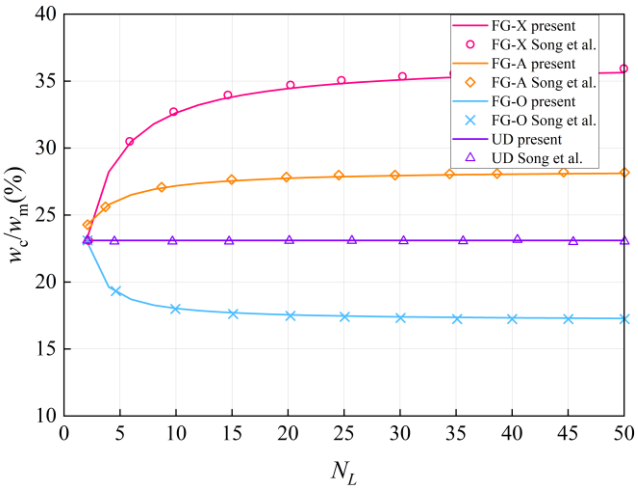

Fig. 5. The connection between the N_L and the percentage change of plate deflection.

5. Comparative analysis

5.1. Comparative analysis of material parameters

Young's modulus, a key indicator of stiffness, is compared across two types of graphene-reinforced composite plates. Based on conclusions from Section 4.3, a layer count of N_L = 25 is selected for the nonporous epoxy-based plates to ensure deflection stability. The plate dimensions are specified as $a = b = 0.2$ m and $h_s = 0.01$ m with the graphene platelets defined as $w_{GPL} = 1.5$ μm, $h_{GPL} = 1.5$ nm, and $l_{GPL} = 2.5$ μm. Unless otherwise stated, all computational parameters default to the values mentioned above.

Numerical results indicate that increasing the number of layers enhances the spatial continuity of FG-O/X distributions around the midplane. The elastic modulus shows

a symmetric, linear gradient across the thickness. A higher number of layers moderately raises the peak Young's modulus relative to N_L = 10. In the FG-X pattern, the top and bottom layers possess the highest graphene content and modulus, while the middle approaches zero. Conversely, FG-O shows maximum modulus and concentration in the central layer. FG-A exhibits a linear increase in modulus from bottom to top, consistent with extreme values in FG-X/O modes.

From Fig. (6), it can be seen that the peak graphene volume fraction of power-law graded graphene reinforced material is greater, and also from Eq. (3), the Young's modulus E and a positively correlated, so the maximum Young's modulus of the power-law graphene reinforced composite is larger than the layered graphene reinforced composite.

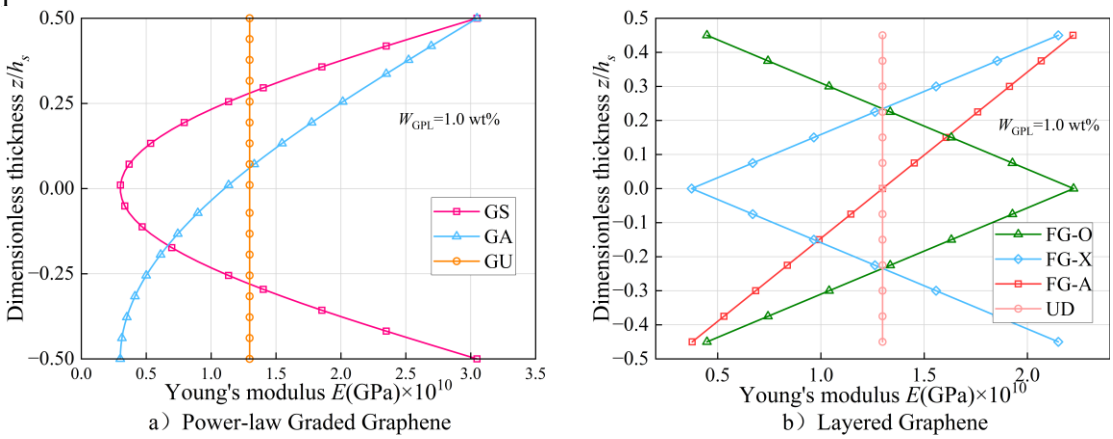

Fig. 6. Young's modulus distribution along the thickness of two graphene-reinforced composite plates.

Accurate thermal conductivity computation is essential for temperature field analysis. Using consistent parameters, this study examines temperature distributions in layered graphene-reinforced composites across four configurations: one non-porous baseline and three characteristic porosity patterns. As shown in Fig. 7(d), the thermal conductivity profile of the non-porous case closely resembles the Young's modulus distribution in Fig. 6(b).

Figs. 7(a)–7(c) present thermal conductivity variations under different porosity configurations and GPL dispersions. Fig. 7(c) shows a consistent decline in thermal conductivity with increasing porosity. Meanwhile, Figs. 7(a) and 7(b) demonstrate that thermal behavior is jointly influenced by GPL arrangement and porosity, aligning with power-law graded materials. Notably, the FG-O pattern shows marked thermal reduction with added porosity, as central graphene enrichment is offset by pore concentration—such combinations should be avoided in design.

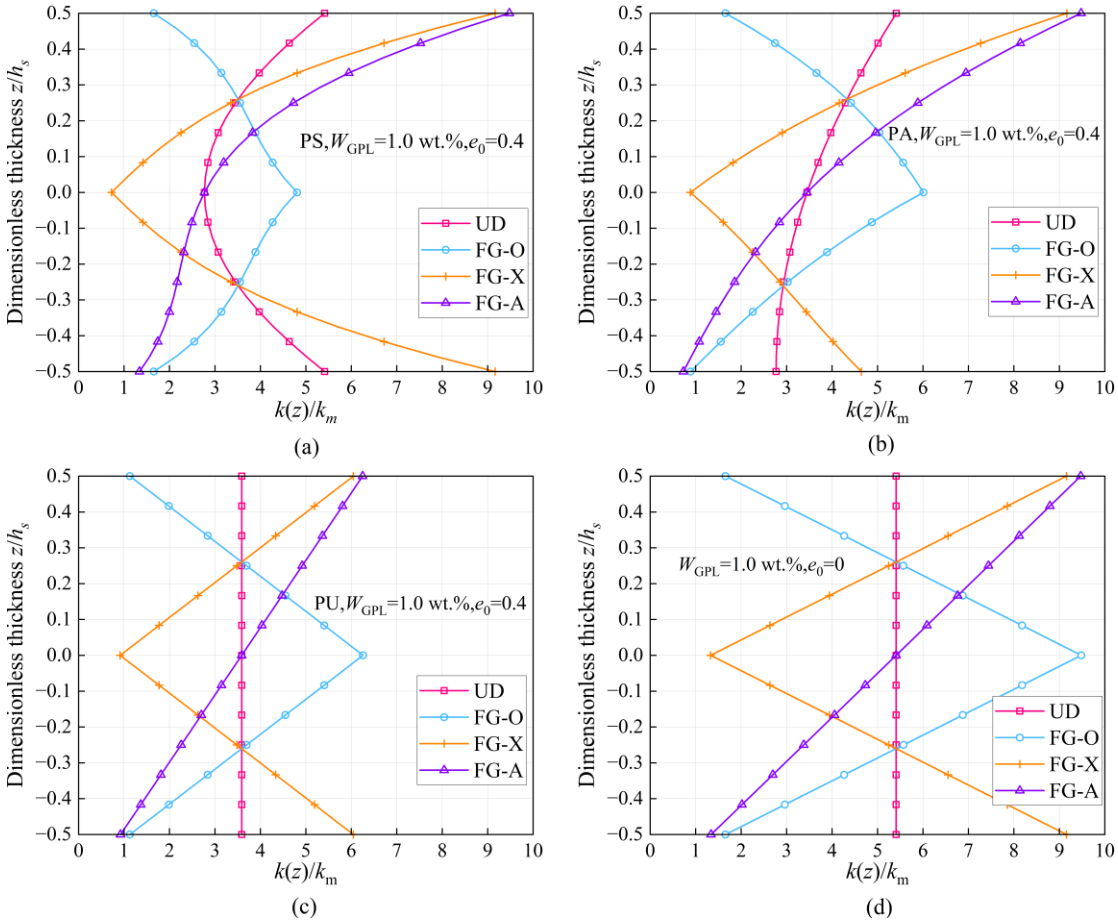

Fig. 7. Thermal conductivity distribution along the thickness direction of multilayer functional gradient graphene reinforced composite sheets.

5.2. Comparative analysis of temperature field distribution

Under top and bottom surface temperatures of 500 K and 300 K, comparative analysis reveals distinct thermal behaviors in plates with different graphene distributions. As shown in Fig. 8, non-uniform GPL dispersions (1.0 wt%) induce nonlinear temperature profiles consistent with power-law gradients. GS shows smoother variation near edges than FG-X; GA changes more gradually top-side but faster bottom-side compared to FG-A, while GU and UD perform identically. These differences result from higher surface conductivity in power-law graded materials versus central conduction in layered composites.

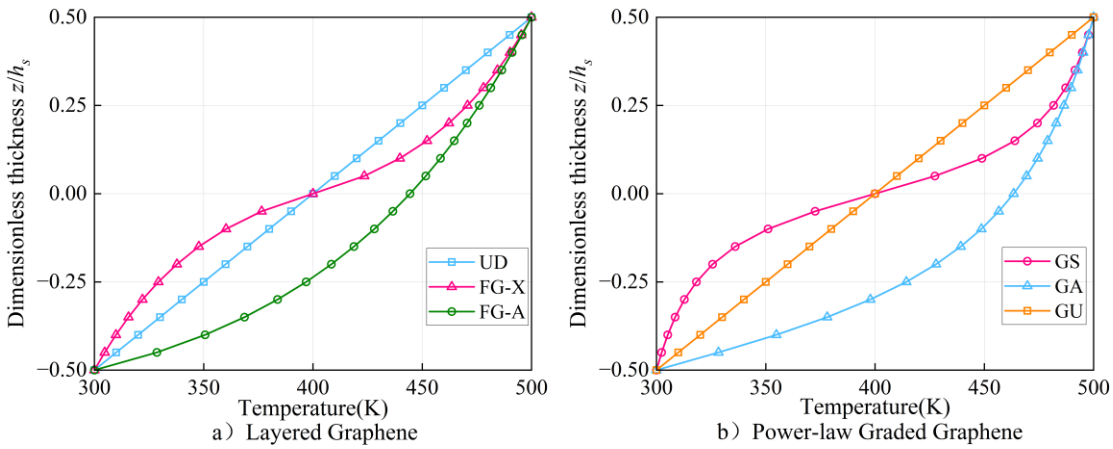

Fig. 8. Temperature distribution of two types of nonporous graphene reinforced composite plates.

5.3. Comparative analysis of static bending

In this section, we compare and analyze the geometric nonlinear static bending responses under mechanical loads of a layered graphene reinforced composite plate and a power-law graded graphene composite platelet. Applying a uniform transverse load of $q_0 = -1\times10^3$ kPa to the epoxy matrix substrate. Fig. 9 compares linear and nonlinear load-deflection responses for porous and non-porous graphene configurations. Among layered composites, FG-X shows the smallest deflection, indicating optimal reinforcement. However, Table 2 reveals that in lightweight plates, GS distribution minimizes central deflection more effectively than FG-X, especially under porous conditions, aligning with Section 5.1. Thus, combining PS and GS is advised for high-strength, lightweight designs. UD and GU distributions exhibit similar effects.

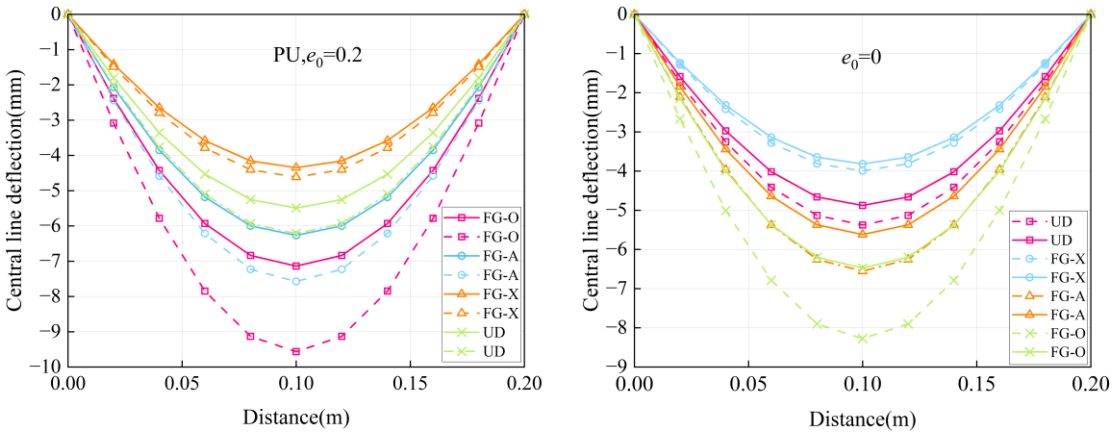

Fig .9. Centerline deflections (solid line is non-linear, dashed line is linear) of different graphene types plates subjected to fixed mechanical loads.

Table 2. Center deflection (mm) of plates with different pores and different graphene distributions

Graphene distribution type	Pore distribution type			
	PS	PA	PU	$e_0 = 0$
Power-law graphene				
GS	-3.6103	-3.7967	-3.8130	-3.3314
GA	-6.6457	-6.8365	-6.7956	-6.1306
GU	-5.2450	-5.4760	-5.5015	-4.8354
Layered graphene				
FG-X	-4.0681	-4.3182	-4.3491	-3.8154
FG-O	-7.0230	-7.1384	-7.1383	-6.4756
FG-A	-6.0771	-6.2374	-6.2673	-5.6178
UD	-5.2372	-5.4680	-5.4935	-4.8762

We also investigated the variation of the center deflection of the nonporous graphene-reinforced composite plate as the load was sequentially increased to 1,000 kPa after five steps. Fig. 10 shows the center deflection curves under different graphene

types, which also proves that the reinforcement of GS is better under the current seven graphene types.

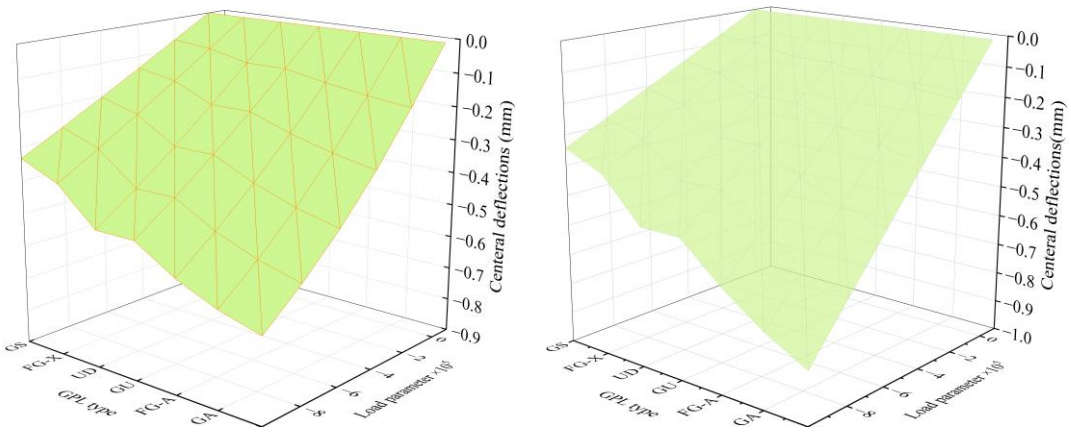

Fig. 10. Deflection change for different graphene distribution types under progressive loading (opaque is nonlinear, transparent is linear)

Fig. 11 provides a detailed comparison of the nonlinear static bending behavior of two types of graphene, illustrating the deflection as the graphene volume fraction increases under a constant mechanical load. From the comparison between Figs. 11(a) and 11(d), it is evident that the incorporation of graphene significantly enhances the stiffness of all plate types. However, introducing pores results in a slight reduction in stiffness, although the stiffness remains higher than that of the initial plate. Furthermore, among the various graphene distributions, the FG-O type exhibits the lowest plate stiffness, whereas the GS type demonstrates the highest, indicating the most effective enhancement.

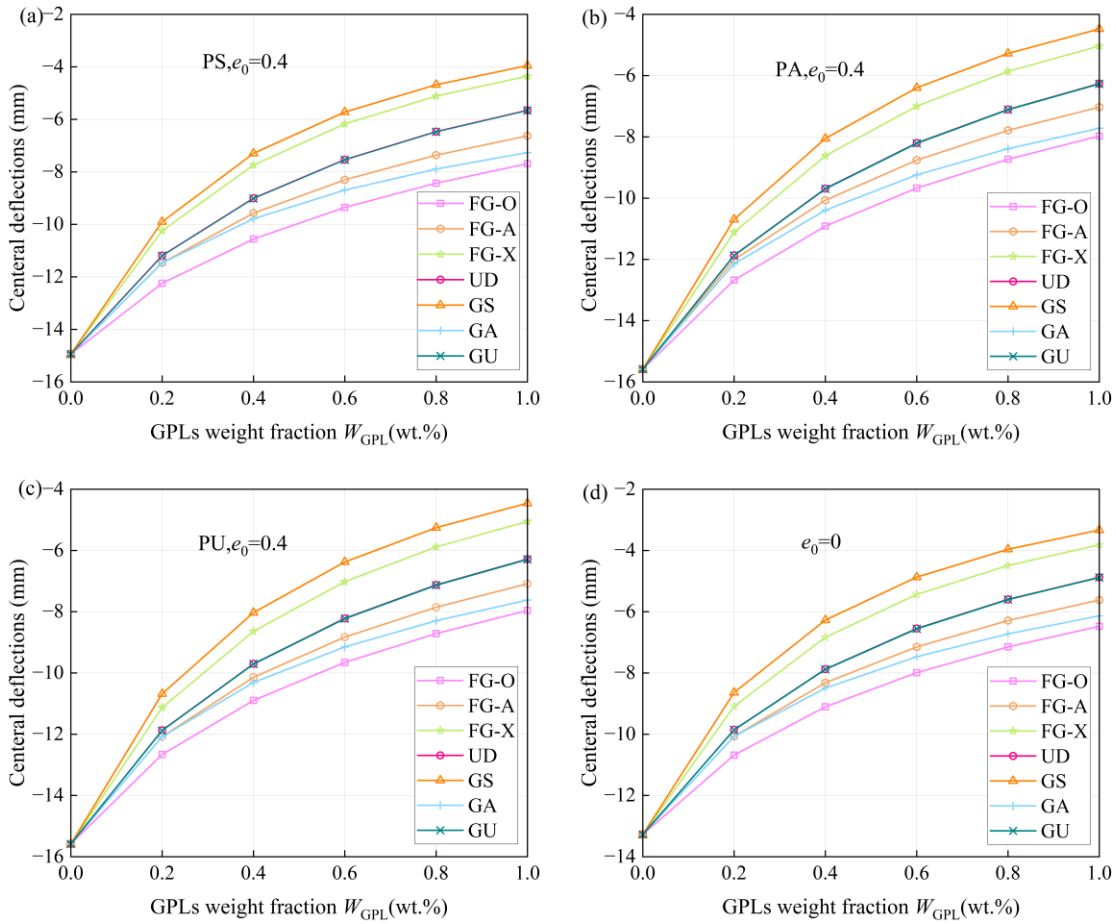

Fig. 11. Comparison of deflection with increasing graphene volume fraction for two types of graphene at a fixed load.

6.Conclusion

This study analyzes the through-thickness thermal conductivity of two graphene-reinforced materials with porosity using S-FSDT and the Maxwell–Eucken model. Nonlinear finite element analysis evaluates static bending, central deflection under incremental loading, and stress distribution. Key conclusions are derived from comparing material and mechanical properties across multiple scenarios.

1)Theoretical derivations show that power-law graded materials provide superior enhancement in Young's modulus across all distribution types.

2）With introduced porosity, the thermal conductivity behavior of FG-A, FG-X, and UD cases resembles that of functional gradient graphene sheet reinforced materials.

3）For lightweight plate applications, the PS-GS combination offers the highest stiffness, followed by PS and FG-X.

References

[1] Lee, Changgu, et al. "Measurement of the elastic properties and intrinsic strength of monolayer graphene." science 321.5887 (2008): 385-388.
[2] Ma, Ruguang, et al. "Multidimensional graphene structures and beyond: Unique properties, syntheses and applications." Progress in Materials Science 113 (2020): 100665.
[3] Zhao, Shaoyu, et al. "Functionally graded graphene reinforced composite structures: A review." Engineering Structures 210 (2020): 110339.
[4] Song, Mitao, Sritawat Kitipornchai, and Jie Yang. "Free and forced vibrations of functionally graded polymer composite plates reinforced with graphene nanoplatelets." Composite Structures 159 (2017): 579-588.
[5] Tao, Chang, and Ting Dai. "Postbuckling of multilayer cylindrical and spherical shell panels reinforced with graphene platelet by isogeometric analysis." Engineering with Computers (2021): 1-16.
[6] Thai, Chien H., et al. "Free vibration, buckling and bending analyses of multilayer functionally graded graphene nanoplatelets reinforced composite plates using the NURBS formulation." Composite Structures 220 (2019): 749-759.
[7] Jin, Qilin, et al. "A refined plate theory for functionally graded carbon nanotube-reinforced plates with piezoelectric actuator." European Journal of Mechanics-A/Solids 90 (2021): 104358.
[8] Nguyen, Van-Loi, et al. "Investigation of static buckling and bending of nanoplates made of new functionally graded materials considering surface effects on an elastic foundation." Acta Mechanica (2024): 1-27.
[9] Zhang Y, Zhu H, Zhao S, et al. Nonlinear dynamic response of functionally graded plates with piezoelectric nonlinearity[J]. European Journal of Mechanics-A/Solids, 2025: 105776.
[10] Van Do, Vuong Nguyen, Thanh Hai Ong, and Chin-Hyung Lee. "Nonlinear thermal buckling analysis of temperature-dependent porous annular and circular microplates reinforced by graphene platelets by using isogeometric analysis method." Engineering Structures 305 (2024): 117738.
[11] Zhang, Yi-Wen, and Gui-Lin She. "Combined resonance of graphene platelets reinforced metal foams cylindrical shells with spinning motion under nonlinear forced vibration." Engineering Structures 300 (2024): 117177.
[12] Zhang Y, Guo X, Wu Y, et al. Active control of cables with piezoelectric actuation considering geometric and material nonlinearities[J]. Engineering Structures, 2025, 340: 120773.
[13] Liu, Tao, et al. "Nonlinear thermal-mechanical coupled isogeometric analysis for GPLs reinforced functionally graded porous plates." Engineering Structures 319 (2024): 118827.
[14] Liu, Tao, et al. "Bi-nonlinear isogeometric analysis of graphene platelets reinforced functionally graded porous plates bonded with piezoelectrics." Composite Structures 306 (2023): 116569.
[15] Chen, Chen, et al. "Thermal vibration analysis of functionally graded graphene platelets-reinforced porous beams using the transfer function method." Engineering Structures 284 (2023): 115963.

[16] Zhang, Yu, et al. "Nonlinear frequency analysis of piezoelectric functionally graded porous plates reinforced by graphene platelets under thermo-electro-mechanical loads." Mechanics of Advanced Materials and Structures (2025): 1-17.
[17] Le Dang Minh, Tu, Thang N. Dao, and Vuong Nguyen Van Do. "Nonlocal nonlinear vibration of porous Graphene Platelets microplates under nonlinear temperature rises using modified couple stress theory based on Bézier extraction of NURBS." Archive ofApplied Mechanics 94.6 (2024): 1807-1827.
[18] Huang, Tianhao, et al. "Free vibration analysis of spinning sandwich annular plates with functionally graded graphene nanoplatelet reinforced porous core." Materials 15.4 (2022): 1328.
[19] Sun, Rui, et al. "Temperature-dependent mechanical properties of defective graphene reinforced polymer nanocomposite." Mechanics of Advanced Materials and Structures 28.10 (2021): 1010-1019.
[20] Song, Mitao, et al. "Thermal buckling and postbuckling of edge-cracked functionally graded multilayer graphene nanocomposite beams on an elastic foundation." International Journal of Mechanical Sciences 161 (2019): 105040.
[21] Song, Mitao, et al. "Free vibration and buckling analyses of edge-cracked functionally graded multilayer graphene nanoplatelet-reinforced composite beams resting on an elastic foundation." Journal of Sound and Vibration 458 (2019): 89-108.
[22] Zhang, Yu, et al. "Nonlinear thermo-electro-mechanical responses and active control of functionally graded piezoelectric plates subjected to strong electric fields." Thin-Walled Structures 205 (2024): 112375.
[23] Guo, Xuankai, et al. "Nonlinear thermo-electro-mechanical analysis of piezoelectric laminated composite beams considering strong electric field." Engineering Structures 325 (2025): 11945.
[24] Zhang, Yu, et al. "Vibration control of membrane structures by piezoelectric actuators considering piezoelectric nonlinearity under strong electric fields." Engineering Structures 315 (2024): 118413.
[25] Nguyen, Van-Loi, et al. "Investigation of static buckling and bending of nanoplates made of new functionally graded materials considering surface effects on an elastic foundation." Acta Mechanica (2024): 1-27.
[26] Zheng, Jie, et al. "On the asymmetric thermal stability of FGM annular plates reinforced with graphene nanoplatelets." Engineering with Computers 38.Suppl 5 (2022): 4569-4581.
[27] Yang, Zhicheng, et al. "Coupled dynamic instability of graphene platelet-reinforced dielectric porous arches under electromechanical loading." Thin-Walled Structures 197 (2024): 111534.
[28] Wu, Yufan, et al. "Active control of cable vibration using piezoelectric actuators considering strong electric field nonlinearity." Journal of Vibration Engineering & Technologies (2024): 1-13.
[29] Reddy J. Analysis of functionally graded plates. Internat J Numer Methods Engrg 2000;47:663–84.
[30] Genao, Francisco Yapor, Jinseok Kim, and Krzysztof Kamil Żur. "Nonlinear finite element analysis of temperature-dependent functionally graded porous micro-

plates under thermal and mechanical loads." Composite Structures 256 (2021): 112931.
[31] Song, Mitao, et al. "Buckling and postbuckling of biaxially compressed functionally graded multilayer graphene nanoplatelet-reinforced polymer composite plates." International Journal of Mechanical Sciences 131 (2017): 345-355.
[32] Zhang Y, Huang Y, Zhao S, et al. Nonlinear dynamic response and stability of piezoelectric shells with piezoelectric nonlinearities[J]. International Journal of Mechanical Sciences, 2025: 110731.

Appendix:

Table 3. Graphene types

GPL distribution type	Symmetric	Asymmetric	Uniform	Corresponding literature
Power-law graded graphene	Pattern A	Pattern B、C	Pattern D	[9]
	GPL – A、GPL - B	~	GPL - C	[11]
	GS	GA	GU	[12][14]
	FGA	FGB	FGC	[17]
	Pattern O、X	~	Pattern U	[18]
	Pattern A	Pattern B	Pattern C	[15]
Layered graphene	FG-X、O	FG-V	UD	[25]
	X、O-GPLRC	~	U-GPLRC	[26]
	~	~	Uniform	[27]

In Eq. (43),

$$\boldsymbol{K}_{uu}=\int_{\Omega}\boldsymbol{B}_{u}^{\mathrm{T}}\boldsymbol{H}_{c}\boldsymbol{B}_{u}\,\mathrm{d}\Omega \tag{44}$$

$$\boldsymbol{K}_{G}=\int_{\Omega}\left(\boldsymbol{B}_{I}^{g}\right)^{\mathrm{T}}\left(\boldsymbol{H}_{c}\hat{\boldsymbol{\varepsilon}}\right)\boldsymbol{B}_{I}^{g}\,\mathrm{d}\Omega \tag{45}$$

$$\boldsymbol{F}_{u}=\boldsymbol{F}_{us}+\boldsymbol{F}_{uc}+\boldsymbol{F}_{ub},\quad \boldsymbol{F}_{ui}=\boldsymbol{F}_{uu} \tag{46}$$

where

$$\boldsymbol{B}_{\mathrm{u}}=\boldsymbol{B}_{\mathrm{L}}+2\boldsymbol{B}_{\mathrm{NL}},\boldsymbol{H}_{\mathrm{c}}=\int_{h}\boldsymbol{H}_{\mathrm{s}}^{\mathrm{T}}\boldsymbol{Q}\boldsymbol{H}_{\mathrm{s}}\mathrm{d}z \tag{47}$$

$$\boldsymbol{F}_{us}=\int_{\Omega}\boldsymbol{N}\boldsymbol{f}_{us}\mathrm{d}\Omega,\boldsymbol{F}_{uc}=\sum\boldsymbol{N}\boldsymbol{f}_{uc},\boldsymbol{F}_{ub}=\int_{\Omega}\boldsymbol{N}\boldsymbol{f}_{ub}\mathrm{d}V, \tag{48}$$

$$\boldsymbol{F}_{uu}=\int_{\Omega}\boldsymbol{B}_{u}^{\mathrm{T}}\boldsymbol{H}_{c}\hat{\boldsymbol{\varepsilon}}\mathrm{d}\Omega, \tag{49}$$